2018

Inception of geohydraulic failures in granular soils - an experimental and theoretical treatment

Buddhima Indraratna
University of Wollongong, indra@uow.edu.au

Jahanzaib Israr
University of Wollongong, jisrar@uow.edu.au

M Li
BC Hydro

Inception of geohydraulic failures in granular soils - an experimental and theoretical treatment

Abstract

This paper outlines an experimental investigation into seepage-induced failures in soils subjected to static and cyclic loading. Internally stable, marginal and unstable soils are characterised by heave, composite heave-piping and suffusion that develops immediately upon instability. In this study, the stable specimens exhibited heave at larger hydraulic gradients than the unstable specimens failing by suffusion at relatively smaller hydraulic gradients. Under no external load (i.e. self-weight only), the relative density (R_d) and particle size distribution (PSD) in tandem controlled the internal stability of soils, although the effective stress magnitude (σ'_{vt}) also had a role to play under both static and cyclic loading conditions. Instability in soils was governed by specific combinations of their geohydro-mechanical characteristics such as PSD, R_d, stress reduction factor, critical hydraulic gradients and associated effective stress levels. These factors are combined to model the development and inception of instability, and the paper offers visual guides as a practical tool for practitioners. Each soil has a unique critical envelope related to its PSD and R_d, and a critical path with its inclination that depends on the hydro-mechanical conditions. The current results of internal erosion tests conducted by the authors plus those adopted from published literature are used to verify the proposed model.

Disciplines

Engineering | Science and Technology Studies

Publication Details

Indraratna, B., Israr, J. & Li, M. (2018). Inception of geohydraulic failures in granular soils - an experimental and theoretical treatment. Geotechnique, 68 (3), 233-248.

Indraratna, B. *et al*. (2018). *Géotechnique* **68**, No. 3, 233–248 [https://doi.org/10.1680/jgeot.16.P.227]

Inception of geohydraulic failures in granular soils – an experimental and theoretical treatment

B. INDRARATNA*, J. ISRAR† and M. LI‡

This paper outlines an experimental investigation into seepage-induced failures in soils subjected to static and cyclic loading. Internally stable, marginal and unstable soils are characterised by heave, composite heave–piping and suffusion that develops immediately upon instability. In this study, the stable specimens exhibited heave at larger hydraulic gradients than the unstable specimens failing by suffusion at relatively smaller hydraulic gradients. Under no external load (i.e. self-weight only), the relative density (R_d) and particle size distribution (PSD) in tandem controlled the internal stability of soils, although the effective stress magnitude (σ'_{vt}) also had a role to play under both static and cyclic loading conditions. Instability in soils was governed by specific combinations of their geo-hydro-mechanical characteristics such as PSD, R_d, stress reduction factor, critical hydraulic gradients and associated effective stress levels. These factors are combined to model the development and inception of instability, and the paper offers visual guides as a practical tool for practitioners. Each soil has a unique critical envelope related to its PSD and R_d, and a critical path with its inclination that depends on the hydro-mechanical conditions. The current results of internal erosion tests conducted by the authors plus those adopted from published literature are used to verify the proposed model.

KEYWORDS: compaction; erosion; filters; gravels; laboratory tests; limit equilibrium methods; permeability; pore pressures; sands; seepage

INTRODUCTION

Granular soils are used as protective filters for erodible cores in embankment dams and natural subgrades in railway sub-structures, because they have excellent drainage and load-carrying characteristics. Filters with appropriate permeability and porosity are selected using empirical guidelines stemming from laboratory observations (Vaughan & Soares, 1982; Fourie *et al*., 1994; Smith & Bhatia, 2010). Nevertheless, these criteria are often overly conservative for uniform soils that are not as abundant as non-uniform or broadly graded natural soils (Li & Fannin, 2008). Although economical for use as filters in dams and railways, natural soils may be susceptible to internal instability whereby seepage dislodges fine particles from the filter voids, hence changing the particle size distribution (PSD), so it can no longer protect the base soil. Previous studies proposed that internal stability was governed by the PSD (Kezdi, 1979; Kenney & Lau, 1985; Lafleur *et al*., 1989), and they also suggested various criteria for selecting stable filters. However, these criteria often eliminate non-uniform soils ($C_u > 6$) as potentially being internally unstable and influence the filter selection towards uniform gradations.

Erodible fines in a non-uniform soil usually take a smaller proportion of external loads than its coarser fraction due to their relative sizes and proportions in the mix. This non-uniformity is described by the stress reduction factor (Taylor *et al*., 2015), as quantified by α, which is defined as the ratio of the magnitude of effective stress in the finer fraction to that of the coarser fraction. Li & Fannin (2012) demonstrated that the factor α can also be given by the ratio of the experimentally observed and Terzaghi's (theoretical) critical hydraulic gradients ($i_{cr,exp}/i_{cr,th}$). The value of α is assumed to be 1 for stable soils where all the particles share in transferring loads due to their equivalent sizes and higher coordination numbers between coarse particles, that is number of neighbouring coarse particles per particle (Scheuermann *et al*., 2010). However, the magnitude of α decreases as the percentage of erodible finer fraction in the soil increases, where the finer particles bear a reduced magnitude of effective stress. Based on hydraulic test data, Skempton & Brogan (1994) related α with the ratio $(H/F)_{min}$ introduced by Kenney & Lau (1985) with a non-linear relationship, where F and H represent percentages finer by mass corresponding to arbitrary sizes d and between sizes d and $4 \times d$ on a PSD curve, respectively. Shire *et al*. (2014) proposed a quadratic relationship between α and fine–coarse coordination number, that is number of neighbouring coarse particles per fine particle. Nonetheless, a clear division between fine (erodible) and coarse (non-erodible) fractions and the R_d of soil are critical factors in determining the exact α values. The percentage of erodible fines in marginally stable soils varies with their R_d and the hydraulic conditions (Israr & Indraratna, 2017). Fig. 1 shows the variations of α with the internal stability index (R_f) described by Indraratna *et al*. (2015), where internally stable uniform soils with $R_f \leq 0{\cdot}7$ possess $\alpha = 1$, while internally unstable soils with $R_f > 0{\cdot}7$ exhibit $\alpha < 1$.

Effective stress in a laboratory soil sample varies due to seepage and boundary friction offered by the walls of the hydraulic cell (Tanaka & Toyokuni, 1991; Moffat & Fannin, 2011). The stress reduction due to seepage and friction leads to the onset of heave in internally stable soils and suffusion in unstable soils. Moreover, boundary friction in the former and inter-particle friction in the latter resists any further

Manuscript received 28 August 2016; revised manuscript accepted 24 May 2017. Published online ahead of print 7 July 2017.
Discussion on this paper closes on 1 August 2018, for further details see p. ii.
* Centre for Geomechanics and Railway Engineering (GRE), University of Wollongong, NSW, Australia.
† University of Engineering and Technology, Lahore, Pakistan; Centre GRE, University of Wollongong, Wollongong, NSW, Australia.
‡ BC Hydro, Burnaby, BC, Canada.

movement of particles at the state of impending instability. For instance, Indraratna *et al.* (2015) reported that the stable soils exhibited heave at $i_{cr,exp} > i_{cr,th}$, possibly due to boundary friction. Skempton & Brogan (1994) reported that instability occurred in soils subjected to vertical flow at $i_{cr,exp}$ much greater than under horizontal flow because of the increased inter-particle contact due to the higher overburden of the soil layer. Seepage failures are governed by specific combinations of effective stress and associated critical hydraulic gradients, i_{cr} (Israr *et al.*, 2016b). Moffat & Fannin (2011) presented empirical correlations between effective stress and critical hydraulic gradients that govern internal instability in soil. Li & Fannin (2008) proposed a normalised stress–gradient plane to interpret the results of piping tests.

This current study purports to shed light on the factors and mechanisms causing the inception of seepage failures in soils. Hydraulic tests were carried out using a modified permeameter apparatus to capture the spatial and temporal variations in average and local porosities, hydraulic gradients and associated effective stresses. Two distinct failure mechanisms were identified at specific combinations of effective stresses and hydraulic gradients, depending on the geometrical characteristics such as particle and constriction size distributions. For instance, heave occurred in internally stable specimens, while their unstable counterparts suffered from suffusion that exacerbated under high-frequency cyclic loading. These mechanisms were modelled theoretically by considering the variations in effective stress due to seepage and boundary friction, stress reduction factor and hydraulic load. A large body of published data and the current results of experiments with internal erosion under static and cyclic loading are used to verify the proposed model.

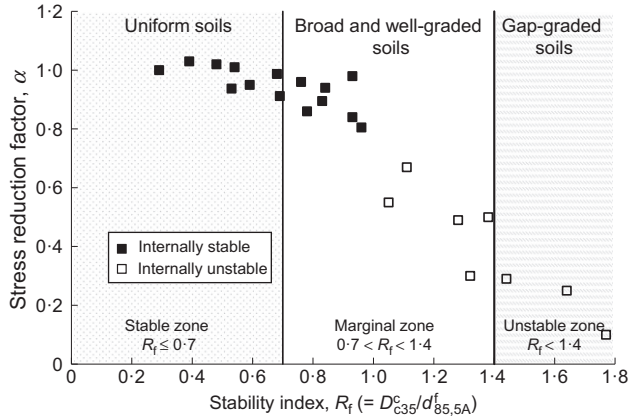

Fig. 1. Variations of stress reduction factor α with the stability index R_f based on experimental results (data from Indraratna *et al.*, 2015)

EXPERIMENTAL PROGRAMME

Test samples, set-up and procedure

As Fig. 2 shows, the test material consisted of a mixture of commercially available crushed basaltic rock and sand that is commonly used for dam filters and railway sub-ballast (Trani & Indraratna, 2010a). The soils for testing were selected based on a two-fold rationale, namely: (*a*) to cover most common soil types used as granular filters in embankment dams and as sub-ballast filters in railway sub-structures; and (*b*) to represent different geo-hydraulic failure types such as suffusion and heave. Under both static and cyclic loading, a total of 32 internal erosion tests were carried out on four different soil gradations ($C_u = 10$–304) – one stable, two marginal and one internally unstable (Indraratna *et al.*, 2015) – under both static and cyclic loading. Following the procedure by Israr *et al.* (2016b), the specimens were compacted at $R_d \geq 95\%$, which could be obtained by controlling the dry mass of soil to achieve a minimum void ratio e_{min} previously determined by preliminary testing (ASTM D4253 (ASTM, 2006)). The pre-determined soil mass was placed in five distinct layers and compacted on a vibrating table (50 Hz frequency) under a 10 kg surcharge for 10 min (Trani & Indraratna, 2010a). The uniformity of these test specimens with respect to compaction and PSD was then ensured by a number of preliminary (trial) tests. For example, additional specimens were prepared using a similar technique and their R_d values were then assessed by determining: (*a*) the overall dry

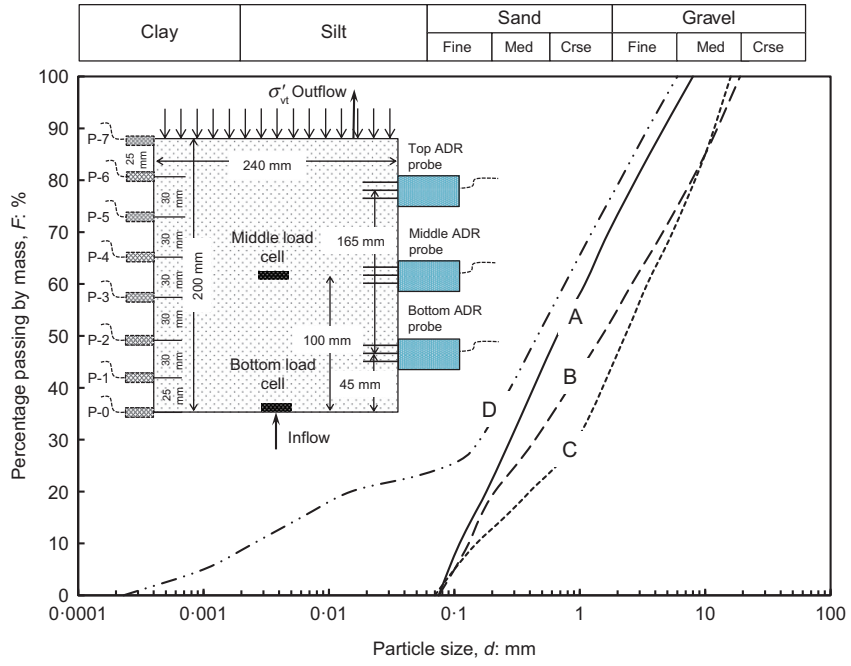

Fig. 2. PSD curves for current test material and schematic illustration of hydraulic test set-up in the inset

density of each specimen, and (*b*) the dry density of small samples cored within each layer of a specimen. By comparing the results of pre- and post-test sieve analyses, the uniformity of tested specimens with respect to the PSD could be examined to establish and ensure acceptable repeatability (Indraratna *et al.*, 2015; Israr *et al.*, 2016a).

During the hydraulic tests, 240 mm dia. saturated specimens (200 mm high) were subjected to the target stress (σ'_{vt}). In the static tests, the magnitude of effective stress ($\sigma'_{vt} = 0$, 25, 50 and 100 kPa) varied, whereas the cyclic tests were conducted under a sinusoidal loading pattern (minimum 30 kPa and maximum 70 kPa and mean = 50 kPa) at frequencies between 5 and 30 Hz. Loading was applied using the same computer-controlled actuator that could apply dynamic loads for a range of frequencies from 0 to 40 Hz (Israr, 2016). Notably, when the frequency was set to zero, static loading was simulated. Using the actuator, the target normal stress was generated from a hydraulic piston and transmitted to the samples through a shaft passing through a frictionless seal at the top boundary of the hydraulic cell and connected to the flexible platen. This loading arrangement induced negligible contact stress reduction ($< 1\%$). During cyclic tests, a continual deviator stress of 40 kPa (i.e. $\sigma'_{min} = 30$ and $\sigma'_{max} = 70$) was applied until the end of testing over a large number of loading cycles (N) from 250 000 to 1 500 000 for the frequency range of 5–30 Hz. Additional details of the loading system are given elsewhere by Israr *et al.* (2016a) and Trani & Indraratna (2010a, 2010b). The physical properties of the test specimens are summarised in Table 1.

According to Zou *et al.* (2013), this cell is large enough to avoid preferential flow channels, and a teflon coating on the inner surface of the cell can minimise boundary friction (Israr *et al.*, 2016b). The reduction in the height of the sample was measured by a linear variable differential transducer (LVDT) displacement gauge (accuracy: 0·05 mm) attached to the top of the specimen and it was used to delineate the final R_d values (Table 1). As Fig. 2 shows, an array of eight differential pore pressure transducers (accuracy: 0·05 kPa) and three amplitude domain reflectometery (ADR) probes (accuracy: 0·05%) were attached along the length of the specimen at pre-requisite intervals to monitor the spatial and temporal hydraulic response (Trani & Indraratna, 2010a, 2010b; Israr & Indraratna, 2017). Two load cells, one in the middle and the other at the bottom of the specimens, facilitated monitoring the variations in total stress over time. The effective stress was deduced from the difference in total stress and pore water pressure obtained by the nearest pore pressure transducer attached to the specimen, which accounted for both the hydraulic (seepage) pressure plus any excess pore pressure developed in the soil specimen.

Notably, these inclusions may modify the assumed one-dimensional geometry of the problem, leading to a non-vertical seepage direction, as well as local heterogeneities that may potentially trigger geo-hydraulic failures. To examine the effects of inclusions, the authors have performed six independent hydraulic tests, that is three with and three without load cells, which constitute up to 2·20% of the total soil volume in a sample compared to the collective volume of ADR probes, wires and transducers ($< 0{\cdot}40\%$), as elaborated earlier by Israr *et al.* (2016b). In essence, the data analysis revealed that the porosity variations before the initiation of instability were uniform and independent of the presence of load cells. Soils exhibited similar hydraulic responses with and without load cells, whereby, for a given soil, seepage failure initiated in the same region and at a unique combination of effective stress and critical hydraulic gradient. This could sufficiently confirm that the presence of load cells had negligible effects on the observed test results.

The test procedure consisted of forcing water from the bottom to the top of the test specimen while controlling the hydraulic gradient (i_a). Initially, a very low magnitude of i_a was applied, for example (0·05 to 0·1) and (0·5 to 1·0) for tests under applied vertical total stress $\sigma_{vt} = 0$ and > 0, respectively. The i_a values were deduced from the external hydraulic pressure across the length of the specimen, h_f (equation (1a)). As indicated on the flow curves in Fig. 3, the local hydraulic gradients i_{ij} were deduced from the differential pressure across a layer of soil (Δy) using equation (1b).

$$i_a = \left(p_w^{in} - p_w^{out}\right)/(h_f \times \gamma_w) \tag{1a}$$

$$i_{ij} = \left(p_w^{i} - p_w^{j}\right)/(\Delta y \times \gamma_w) \tag{1b}$$

The system was allowed to attain steady flow conditions with no significant changes to the internal hydraulic pressures for a sustained period of time before the next increment of i_a was applied. Each specimen was subjected to upward flow until the critical onset; that is, a point corresponding to the inception of seepage failure, as characterised by suffusion, visual heave, or until the hydraulic capacity of the water pump was reached. Variations in porosity were monitored by ADR probes, while local hydraulic gradients from differential pore pressure readings and effluent flow rates and turbidity histories (nephelometric turbidity unit, NTU $\gg 60$) by way of two data loggers (PCMaster and dataTaker) enabled consistent observations of critical onsets (Israr *et al.*, 2016b). The samples were retrieved in three layers for post-test PSD analysis and to estimate the amount of eroded fines. An unstable soil could be characterised by large variations in its post-test PSD curve and C_u value (Indraratna *et al.*, 2016), whereas the net amount of fines washed out from the middle (f_c), and those from the overall test specimen (f_t) were separately obtained (see Table 1). The post-test reduction in specimen height (s_t) due to mass loss and the volumetric compression due to the applied σ_{vt} and cyclic loading were recorded.

TEST RESULTS AND DISCUSSION

Hydraulic response under static and cyclic loading

Figure 3 shows the variations of effluent flow rates (Q_e in l/min) and turbidity (T_e in NTU), with the hydraulic gradient (i_a) for sample B, under static and cyclic loading. The critical onsets of heave or suffusion were characterised by marked variations in the slopes of the flow curves, increased effluent turbidity ($\gg 60$ NTU) and visual signs of heave or washout; the corresponding values of i_a were assumed as the average critical hydraulic gradient, $i_{cr,a}$ (e.g. Moffat & Fannin, 2011; Indraratna *et al.*, 2016). During the static tests, specimens B exhibited heave with an effluent turbidity well below 60 NTU before the critical onset ($i_a \leq$ observed critical hydraulic gradient, $i_{cr,a}$). The magnitude of $i_{cr,a}$ increased proportionally with the static vertical total stress ($\sigma_{vt} = 0$–100 kPa), thus showing the effects of stabilisation as reduced effluent turbidity and erosion (Fig. 3(a)). However, the cyclic loading proved to be destabilising, and this increased at higher cyclic frequencies (f in Hz), for example soil B experienced suffusion, which increased markedly at $f = 20$ and 30 Hz, yielding permanent changes in its PSD curve. The magnitudes of $i_{cr,a}$ decreased with increase in f (from 0 to 30 Hz) which disturbed the fines and constriction network due to increased agitation, resulting in increased erosion, that is $T_e \gg 60$ NTU (Fig. 3(b)). Cyclic loading may lead to suffusion instead of heave failure with larger amount of eroded fines, that is higher effluent turbidity.

Table 1. Summary of physical soil properties and laboratory test results for current study

Test number	Sample ID	Test condition	Central layer, C_u		σ_{vt}: kPa	$\sigma'_{mv,ij}$: kPa	α	$i_{cr,a}$	$i_{cr,ij}$	$i_{\Delta u}$	Eroded fines: %		s: %	k_s: $\times 10^{-4}$ m/s	R_d: %	Failure type	Internal stability
			Pre-test	Post-test							Total sample (f_t)	Mid-layer (f_c)					
1	A-S-0	Static	10	10	0	0	1	1·14	1·19	—	0·03	0	0·85	2·04	96	Heave	Yes
2	A-S-25		10	10	25	2	1	12·8	12·8	—	0·027	0	1·04	1·94	96	Heave	Yes
3	A-S-50		10	10	50	6	1	28·5	35·6	—	0·015	0	0·71	1·77	97	Heave	Yes
4	A-S-100		10	10	100	9	1	53·4	52·7	—	0·013	0	0·93	1·54	96	Heave	Yes
5	B-S-0		23	23	0	0	0·8	1·06	1·03	—	2·53	1·81	0·8	1·36	97	Heave	Yes
6	B-S-25		23	23·1	25	4·5	0·8	14·1	12·8	—	2·32	1·7	1·13	1·24	98	Heave	Yes
7	B-S-50		23	23	50	9	0·8	26·9	24·6	—	1·71	1·54	1·11	1·17	97	Heave	Yes
8	B-S-100		23	23	100	15	0·8	42·5	40·3	—	1·22	1·75	1·12	1·02	96	Heave	Yes
9	C-S-0		20	20·06	0	0	0·7	0·94	0·98	—	3·81	3·37	0·99	1·27	98	Heave	Yes
10	C-S-25		20	20·11	25	5·5	0·7	14·1	15·2	—	3·05	3·52	1·06	1·19	98	Heave	Yes
11	C-S-50		20	19·94	50	11	0·7	19·5	29·6	—	2·83	2·84	1·11	1·13	96	Heave	Yes
12	C-S-100		20	19·94	100	17·8	0·7	42·5	47·4	—	2·51	2·92	1·06	1·09	95	Heave	Yes
13	D-S-0		304	90	0	0	0·18	0·26	0·23	—	7·37	6·26	2·01	0·042	97	Suffusion	No
14	D-S-25		304	52·94	25	10·1	0·18	5·1	9·69	—	8·33	6·59	1·9	0·036	98	Suffusion	No
15	D-S-50		304	58·33	50	23·2	0·18	13·1	21·9	—	7·91	6·62	1·93	0·027	99	Suffusion	No
16	D-S-100		304	43·33	100	45·4	0·18	25·5	42·6	—	8·89	7·39	1·93	0·012	98	Suffusion	No
17	A-C-5	Cyclic	10	9·97	—	8·5	1	50·5	49·8	5·9	0·22	0	1·25	1·83	97	Heave	Yes
18	A-C-10		10	9·98	—	9·2	1	42·2	53·8	6·3	0·19	0	1·38	1·74	97	Heave	Yes
19	A-C-20		10	10·11	—	10·2	1	38·9	59·5	6·8	0·26	0	1·4	1·7	96	Heave	Yes
20	A-C-30		10	10·2	—	11·9	1	34·5	69·2	7·7	0·3	0	1·45	1·65	98	Heave	Yes
21	B-C-5		23	17·52	—	9·5	0·8	32·1	25·9	3·1	4·11	3·17	1·68	0·95	97	Suffusion	No
22	B-C-10		23	17·19	—	8·75	0·8	30·5	23·9	2·8	4·33	3·34	1·81	0·90	96	Suffusion	No
23	B-C-20		23	16·72	—	10·8	0·8	28·9	29·3	3·7	4·52	3·61	1·93	0·86	97	Suffusion	No
24	B-C-30		23	16·75	—	12·1	0·8	25·5	32·7	4·3	4·76	3·56	2	0·83	98	Suffusion	No
25	C-C-5		20	16·83	—	12·75	0·7	26·8	34·2	10·5	5·17	3·82	2·01	1·1	98	Suffusion	No
26	C-C-10		20	15·33	—	15·6	0·7	26·1	41·7	12·7	5·49	4·07	2	1·02	97	Suffusion	No
27	C-C-20		20	16·89	—	17·5	0·7	25·1	46·7	14·1	5·73	3·76	1·95	0·94	96	Suffusion	No
28	C-C-30		20	15·96	—	21·8	0·7	23·85	57·9	14·9	5·93	4·28	1·93	0·88	98	Suffusion	No
29	D-C-5		304	28·13	—	36·7	0·18	29·4	34·5	12·5	12·16	11·54	2·24	0·021	97	Suffusion	No
30	D-C-10		304	25·04	—	39·9	0·18	28·2	37·5	13·5	13·55	12·26	2·22	0·017	98	Suffusion	No
31	D-C-20		304	30·02	—	44·4	0·18	26·3	41·7	15·1	13·96	12·33	2·28	0·011	99	Suffusion	No
32	D-C-30		304	34·96	—	46·1	0·18	24·7	43·3	15·7	14·23	12·85	2·33	0·010	99	Suffusion	No

Note: Here, (A-B-C), R_d, α, C_u, k_s, s, σ_{vt}, $\sigma'_{mv,ij}$, $i_{cr,a}$ and $i_{cr,ij}$ represent sample identity, relative density, stress reduction factor, coefficient of uniformity, saturated permeability, post-test settlement of samples, applied vertical total stress, mean vertical effective stress in critical soil layer, average critical hydraulic gradient and local critical hydraulic gradient, respectively (A = test soil (see Fig. 5), B = test condition (static/cyclic) and C = loading magnitude (kPa)/loading frequency (Hz)). During cyclic tests, loading cycles of $\sigma_{min} = 30$ kPa, $\sigma_{max} = 70$ kPa and $\sigma_{v,mean} = 50$ kPa were applied.

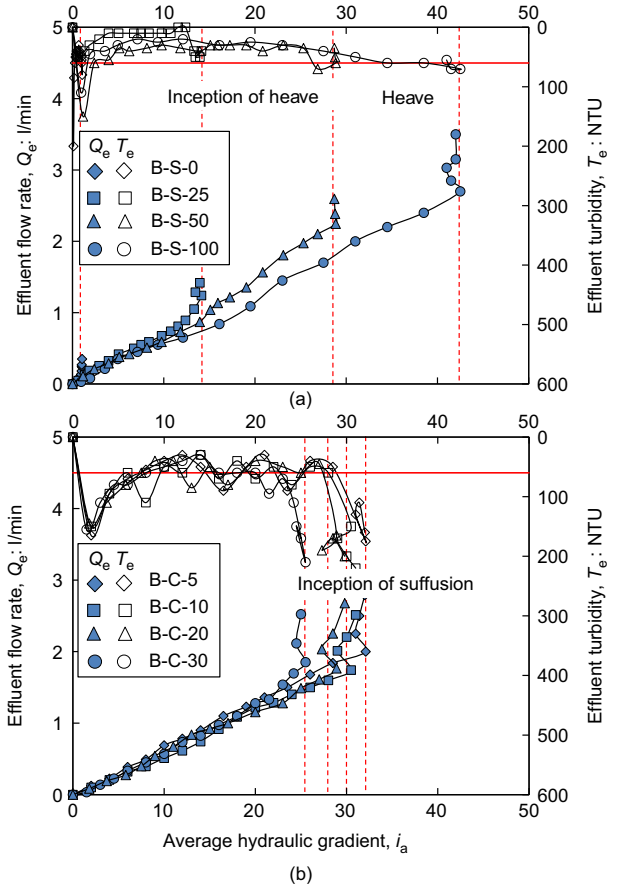

Fig. 3. Variations of effluent flow rate and turbidity against average hydraulic gradient for sample B under: (a) static (i.e. tests B-S-0, B-S-25, B-S-50 and B-S-100) and (b) cyclic loading (tests B-C-5, B-C-10, B-C-20 and B-C-30)

Variations of local porosity in stable and unstable specimens

Figure 4 presents the time histories of variations in local porosity as captured by the top, middle and bottom ADR probes. Irrespective of static or cyclic load, samples A and D exhibited heave and suffusion under upward flow, respectively. Not surprisingly, the cyclic densification of the specimens incurred sudden reduction in porosity and hence permeability (e.g. Trani & Indraratna, 2010b). Following this, porosity remained uniform prior to the onset of heave, where the porosity in the critical layer 12 (i.e. 25–55 mm from the bottom) increased rapidly, while that in the subsequent layers decreased (Figs 4(a) and 4(b)). Tighter packing between particles (coarse–coarse, coarse–fine and fine–fine) of internally stable sample A did not allow erosion to occur, whereas there were marked variations in porosity before suffusion commenced in sample D. The internal erosion increased further at the onset of suffusion, and then later, as shown in Figs 4(c) and 4(d). During static tests, there were no significant variations in porosity prior to the occurrence of heave or suffusion. However, the agitation from the cyclic load may have caused rearrangements of voids of the stable coarse fraction (Xiao *et al.*, 2006), causing further erosion of fines which were trapped within the pore spaces, as shown by the internal porosity curves presented in Figs 4(c) and 4(d).

Time histories of local hydraulic gradients and the critical onset of failure

Local head losses from internal porosity in seven distinct layers of samples were monitored using an array of pore pressure transducers. Fig. 5 shows the time histories of local hydraulic gradients (i_{ij}) that were deduced from the head losses from tests on sample D under static and cyclic loading. A critical onset of suffusion could be characterised by a sudden drop in the local hydraulic gradient, and the corresponding value of i_{ij} was considered to be the local critical hydraulic gradient $i_{cr,ij}$ (Moffat & Fannin, 2011), and is identified on each plot with the corresponding average critical hydraulic gradient $i_{cr,a}$ and the type of seepage failure. For instance, the unstable sample D experienced suffusion, which became excessive under cyclic loading compared to the static tests (Figs 5(a) and 5(b)). Suffusion occurred at a relatively larger $i_{cr,ij}$ but smaller $i_{cr,a}$ values, but nearly twice as much erosion occurred under cyclic loading compared to the static loading tests (see Table 1). The additional hydraulic gradient ($i_{\Delta u}$) due to excess pore water pressure (Δu) under cyclic loading plus i_{ij} from external hydraulic pressure may have resulted in the development of critical onset (e.g. Israr *et al.*, 2016b). At such critical onsets, the $i_{\Delta u}$ would be given by $(h_w^t - H_w^t)/h_f$, where h_w^t, H_w^t and h_f define the sum of internal head losses measured across the differential pore pressure transducers, external head loss measured across the inflow and outflow transducers and the depth of sample, that is 200 mm, respectively (Israr, 2016).

Upward flow caused heave or suffusion to develop over time, which corresponded fully with their critical onsets observed from the analysis of flow, turbidity and porosity curves presented previously. At the point when these onsets began, permeability increased due to erosion during suffusion and the development of horizontal channels during heave that reduced the loss of head, as indicated by a marked drop in i_{ij} histories. An analysis of the internal and external head losses (i_{ij} and i_a) could obtain the value of $i_{\Delta u}$, reported in Table 1. During the static tests there was no internal pore pressure and the erodible fines remained generally intact prior to the critical onsets. However, under cyclic loading, the histories of i_{ij} showed the development of pore pressure, whose magnitude increased with the frequency of loading. For instance, the magnitudes of $i_{cr,a}$ decreased, whereas those of $i_{cr,ij}$ increased significantly with the increase in cyclic loading frequency. Similarly, the $i_{cr,ij}$ values for cyclic tests at applied mean total stress, $\sigma_{v,mean} = 50$ kPa were comparatively higher than those obtained from static tests at $\sigma_{vt} = 50$ kPa (see Table 1).

Seepage-induced variations of effective stress distribution in specimens

Figure 6 shows the spatial distribution of vertical effective stress (σ'_v) with depth when sample B was subjected to static and cyclic loading, that is tests 5–8 (Fig. 6(a)) and tests 21–24 (Fig. 6(b)), respectively. For brevity, only the stress distributions measured at the start of the test (filled symbols) and at the critical onset of heave or suffusion (hollow symbols) are illustrated. The stress decreased with the sample depth due to boundary friction initially and then due to a combination of upward seepage and friction until the occurrence of critical onset. The sample B developed heave with negligible erosion under static loading and observed to be internally stable, but it did suffer from extensive erosion (suffusion) under cyclic loading and thereafter deemed unstable. Interestingly, instability developed in the same layer 23 (55–85 mm from the bottom of the specimen) during all the tests on sample B, where stress at the critical onset of instability was less than 10 kPa during static tests, while up to 19 kPa during cyclic tests, indicating premature failure under cyclic loading.

Figure 7 shows the type of seepage failures in selected test samples A and D. Regardless of the loading condition,

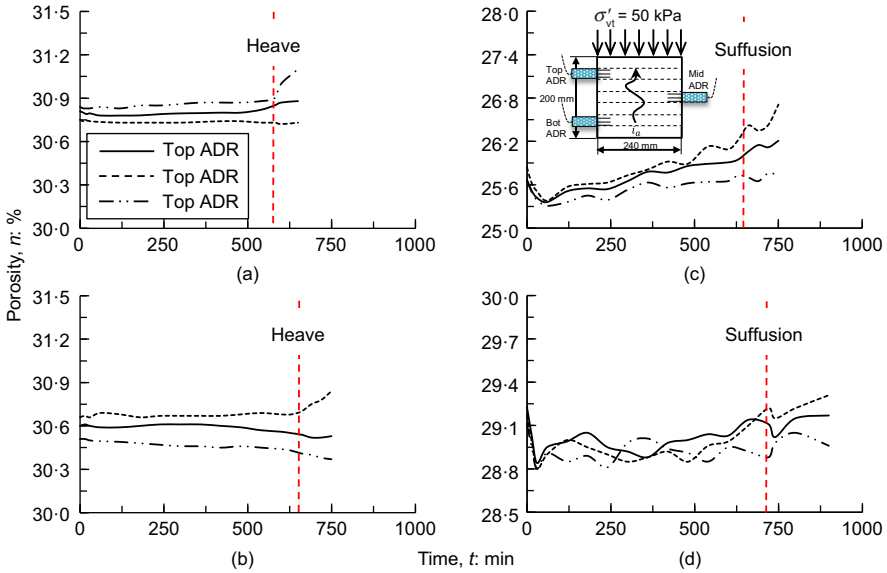

Fig. 4. Porosity variations for the selected samples A and D under static and cyclic loading: (a) test A-S-0; (b) test A-S-25; (c) test D-C-10; (d) test D-C-30

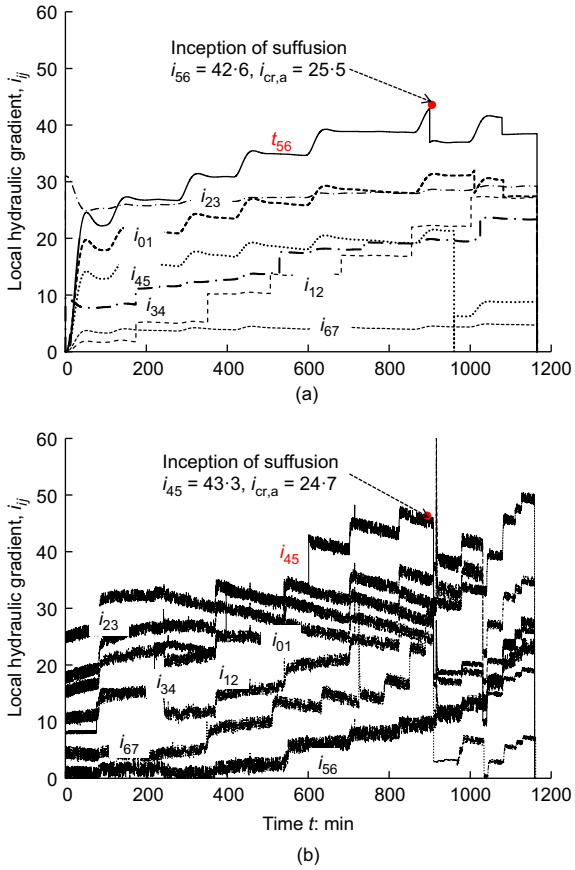

Fig. 5. Time histories of local hydraulic gradients for select sample D under: (a) static loading (test D-S-100) and (b) cyclic loading (test D-C-30)

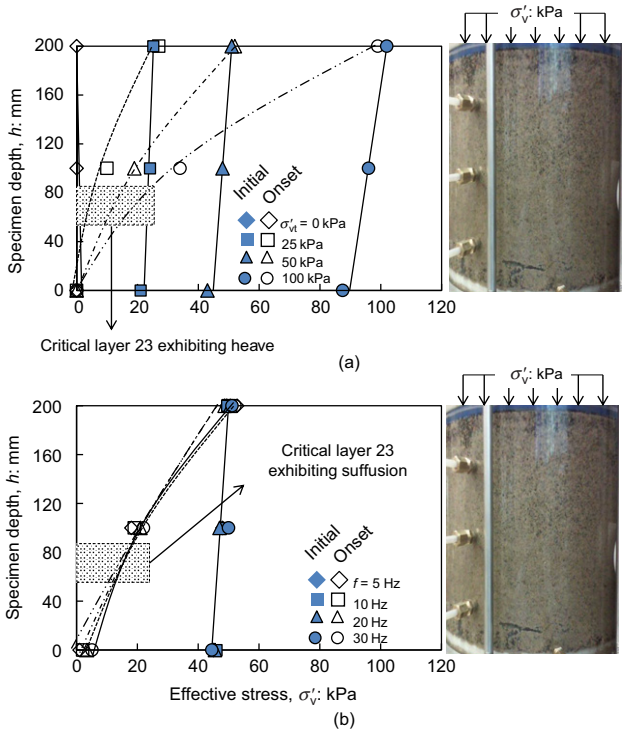

Fig. 6. Initial and final (i.e. at the critical onset) effective stress variations with depth in sample B under (a) static and (b) cyclic loading

A exhibited heave with negligible erosion, while D suffered from suffusion, and they were characterised as internally stable and unstable, respectively. The marginal samples B and C showed limited erosion before developing heave under static loading (i.e. stable), but they experienced an excessive washout of fines under cyclic loading, hence internally unstable.

Table 1 presents the normal stresses at critical onsets of instability (i.e. heave or suffusion) with the associated values of $i_{cr,a}$ and $i_{cr,ij}$. Note that these critical onsets in static tests were reached as the corresponding initial stresses decreased by almost 95%, whereas under a cyclic load the instability commenced with less than 80% initial stress reduction. For instance, the critical onsets in A-S-50 (heave) and C-C-5 (suffusion) occurred at initial magnitudes of $\sigma'_{vt} = 49$ and 47 kPa, and final magnitudes of $\sigma'_{vt} = 6$ (88% reduction) and 14 kPa (64% reduction), respectively. Given that the magnitude of σ'_{vt} for sample C corresponding to the critical onset under cyclic loading was higher than under static loading, a

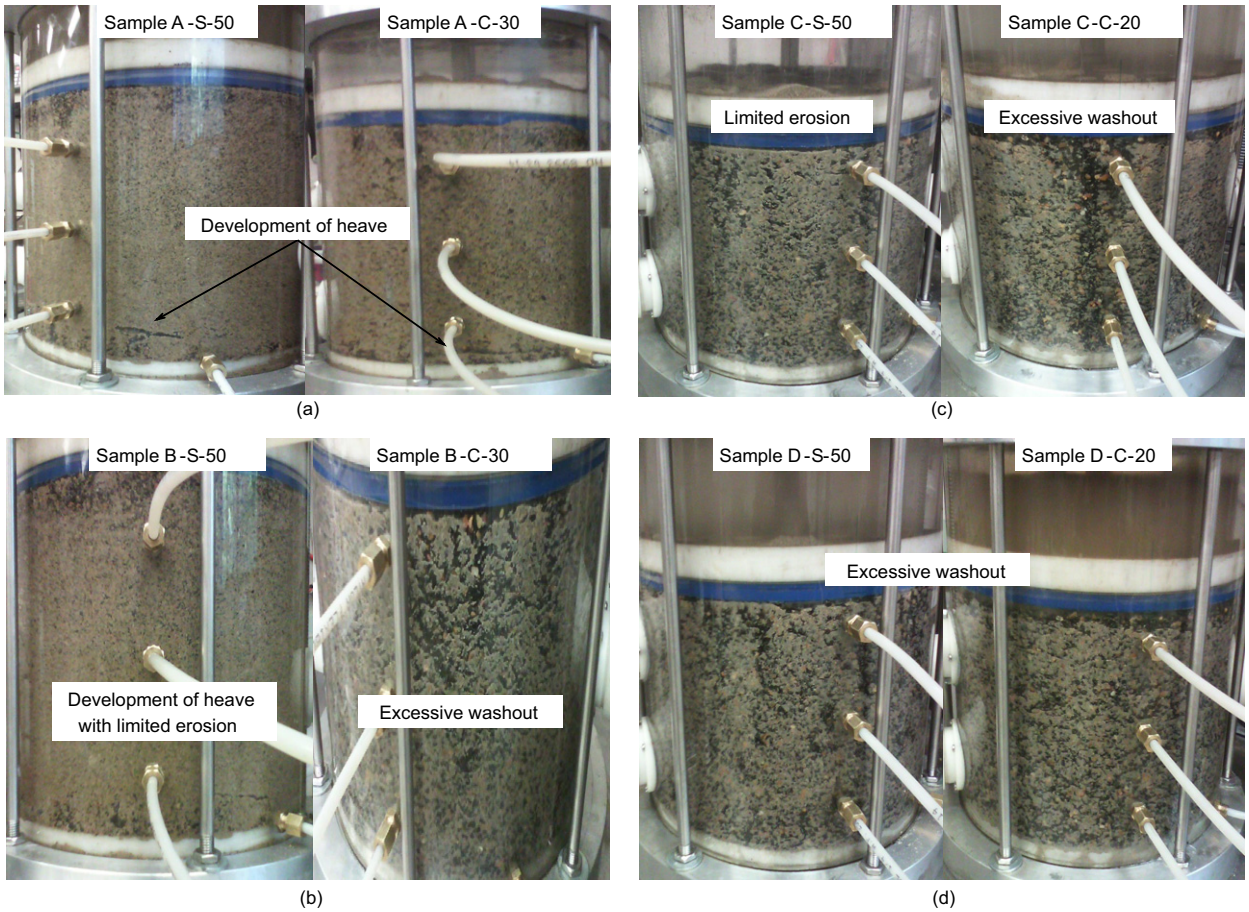

Fig. 7. Illustrations of seepage-induced failures in current test specimens under static and cyclic loading

larger magnitude of i_{cr} would be needed to develop internal instability. Similarly, a comparison between the values of $i_{cr,a}$ and $i_{cr,ij}$ revealed that the ratio $i_{cr,ij}/i_{cr,a}$ under static loading varied between 0·8 and 1·7, and it varied from 1·3 to 2·1 under cyclic loading. This shows that, unlike an externally applied i_a during static tests, the $i_{cr,ij}$ under a cyclic load stemmed from both accumulated Δu and i_a. Not surprisingly, the magnitude of Δu (hence $i_{\Delta u}$) was observed to be the functions of the cyclic stress magnitude, frequency and initial permeability reduction due to densification (see Table 1). As Fig. 8 shows, the magnitudes of $i_{cr,ij}$ and associated mean effective stresses ($\sigma'_{mv,ij}$) in the critical soil layer could be defined by unique correlations for all the test samples, regardless of the loading condition.

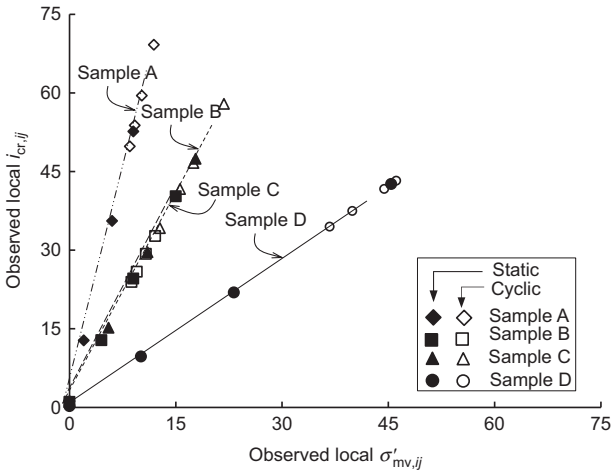

Fig. 8. Local critical hydraulic gradients plotted against mean effective stress magnitudes at the critical onsets

Mechanisms of seepage failures in internally stable and unstable soils

Figure 9 presents the mechanisms of seepage-induced failures in internally stable and unstable specimens observed for the current tests. An internally stable soil develops heave at larger hydraulic gradients that may be accompanied with some limited erosion (< 4%) from its surface which is too small to induce any permanent changes to its original PSD, as shown in Table 1. However, an internally unstable soil experiences washout of its fines at relatively smaller hydraulic gradients that changes its PSD. Erodible fines in an unstable soil barely share mechanically active contacts with the stable load-carrying coarse particles (Langroudi *et al.*, 2013; Shire *et al.*, 2014), therefore, inter-particle contact friction at the onset of suffusion is smaller than the boundary friction that enables individual fines to erode rather than the whole soil column fail due to heave. Once the geometrical requirement is met, that is, erodible particle < controlling constriction (e.g. Indraratna *et al.*, 2015), suffusion is triggered, whereby the drag forces dislodge fine particles from the pore spaces well before the hydraulic forces could lift the whole specimen to induce heave. In contrast, inter-particle friction due to mechanically active contacts between the neighbouring particles of an internally stable soil is greater than the boundary friction offered by the cell walls when the soil column is lifted up by seepage during

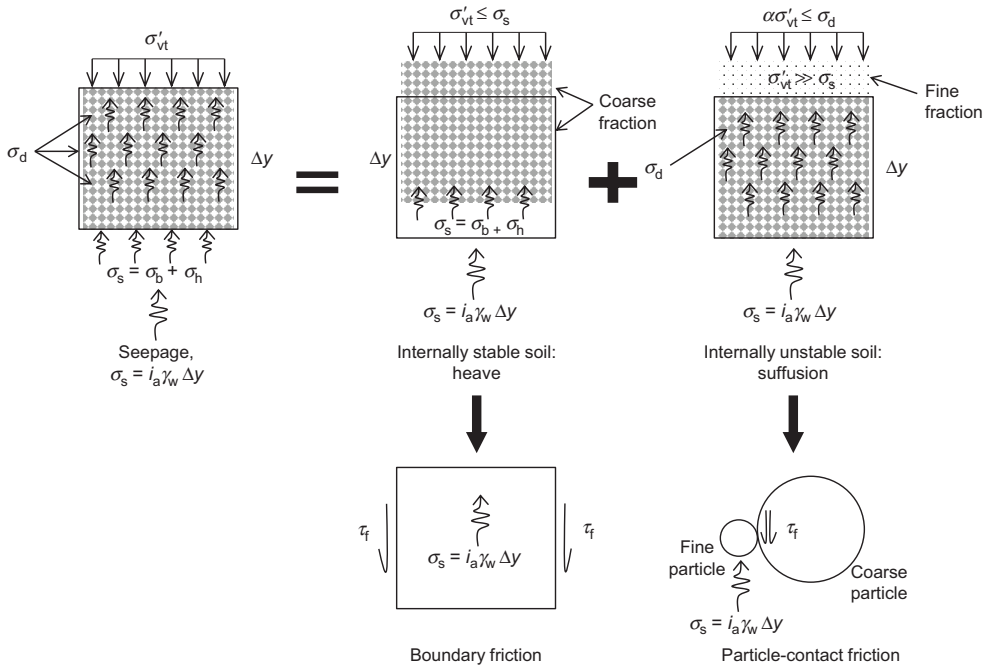

Fig. 9. Mechanisms of seepage-induced failures or internal instability in granular soils

heave (e.g. in Figs 7 and 8). Meanwhile, hydrodynamic forces neutralise wall–particle friction well before the inter-particle contacts ($i_{cf} \ll i_{pf}$) are lost, which eventually results in the development of heave, as also observed in earlier studies by Moffat & Fannin (2011) and Tanaka & Toyokuni (1991).

Figure 10 presents the analysis of seepage-induced reduction of stress in the finer fraction for samples A (stable) and D (unstable). The magnitudes of drag (σ_d), buoyancy (σ_b) and hydro-dynamic (σ_h) stresses were computed using the mathematical expressions indicated in Fig. 10. During heave in A, the seepage stress was greater than the effective stress carried by the particles, that is ($(\sigma_h + \sigma_b) > \alpha\sigma'_{ij}$), while the drag on fine particles evolving from internal head losses due to reduction in permeability was still very small (Fig. 10(a)). In contrast, Fig. 10(b) shows that the drag was greater than the effective stress carried by the erodible fines of sample D when suffusion began (i.e. $\sigma_d > \alpha\sigma'_{ij}$ in fines), while the associated σ_h and σ_b were very small.

THEORETICAL MODEL FOR THE INCEPTION OF HEAVE AND SUFFUSION

In a controlled volume of soil ($\Delta x \times \Delta y \times \Delta z$) subjected to upward flow due to a seepage force (F_s) under a hydraulic gradient (i), the equilibrium requires balance between the disturbing (seepage) and the stabilising (σ'_{mv} including self-weight of soil) constraints, that is

$$i\gamma_w \Delta x \Delta y \Delta z = (\sigma'_{mv} \Delta x \Delta z) \times K_g \quad (2)$$

where K_g is a geometric factor that is unique for a soil and depends upon its PSD, R_d and the frictional characteristics. Its value tends to be unity for internally stable soils (e.g. uniform), but it is expected to be smaller for unstable soils (Skempton & Brogan, 1994). The value of $i_{cr,0}$ observed in a laboratory piping test can be an acceptable estimate of factor K_g that may be represented as a combined function of the stress reduction factor (α), frictional resistance and i_{c0} obtained from the piping theory of Terzaghi (1939). Based on the experimental results, the critical hydraulic gradient for

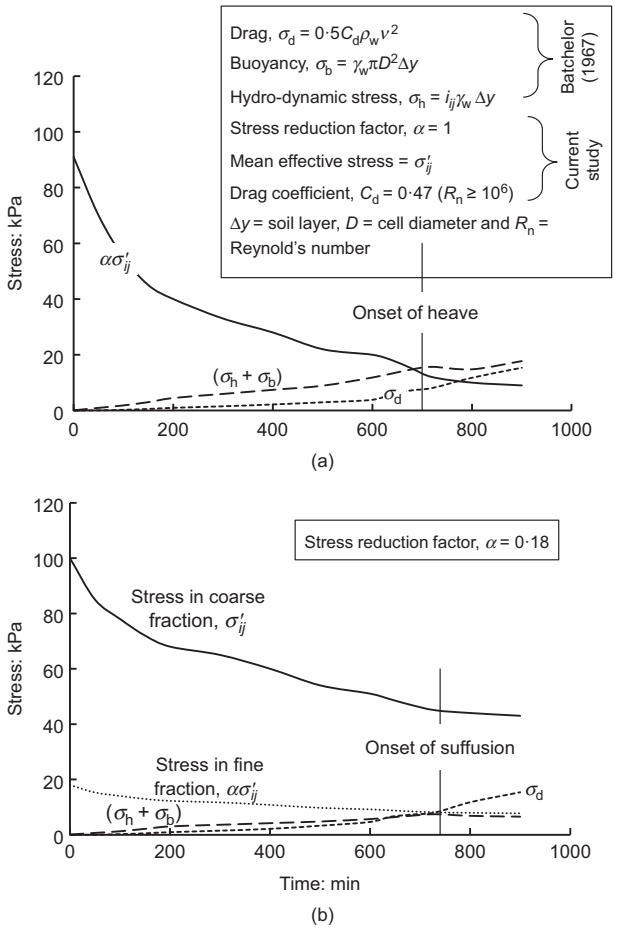

Fig. 10. Seepage-induced effective stress reduction analysis for samples A and D: (a) development of heave in test A-S-100; (b) development of suffusion in test D-S-100

internal instability in soils under self-weight with the effect of friction (i.e. inter-particle or boundary) is given by

$$i_{cr,0} = \alpha \times [(G_s - 1)/(1 + e)] + i_{i,f} \quad (3)$$

where $i_{i,f}$ is the additional hydraulic gradient due to friction that depends on the type of seepage failure, as discussed in the last section. For instance, an internally stable specimen failing in heave would require the consideration of the effects of boundary friction, whereas its counterparts would need to consider inter-particle friction. If the effects of inter-particle and boundary friction are quantified in terms of additional hydraulic gradients (i_{pf} and i_{cf}), then the $i_{i,f}$ in equation (3) should be substituted by i_{pf} and i_{cf} for internally stable and unstable soils, respectively. So by rearranging equation (2), the critical hydraulic gradient for piping in soils subjected to additional mechanical loading (σ'_{mv}) reads

$$i_{cr,p} = \sigma'_{mv} \times i_{cr,0}/\gamma_w \Delta y \tag{4}$$

The critical hydraulic gradient (i_{cr}) for internal instability is given by the sum of $i_{cr,0}$ (for self-weight only) and $i_{cr,p}$ (for external load)

$$i_{cr} = i_{cr,0}\left(1 + \frac{\sigma'_{mv}}{\gamma_w \Delta y}\right) \tag{5}$$

$$i_{cr} = \left\{\alpha \times [(G_s - 1)/(1 + e)] + i_{i,f}\right\}\left(1 + \frac{\sigma'_{mv}}{\gamma_w \Delta y}\right) \tag{6}$$

In Fig. 11, the experimentally observed ($i_{cr,exp}$) and predicted ($i_{cr,p}$) critical hydraulic gradients are plotted with data adopted from existing studies, where most of the points plot along the line of equality; this shows a close agreement with the theory (±7% standard deviation). The following sections briefly describe how the model parameters, including α, $i_{i,f}$ and σ'_{mv}, were determined.

Stress reduction factor

Stress decreases when erodible fines are too small to form a mechanically active contact (load-transferring) with the particles which constitute the stable constriction network (Langroudi *et al.*, 2013; Shire & Sullivan, 2013). The retention ratio, $R_f (= D^c_{c35}/D^f_{85,SA})$ is an acceptable measure of demarcation between stable and erodible soil fabrics (Indraratna *et al.*, 2016). In this study, the following empirical relation that correlates α and R_f was used based on the data by Indraratna *et al.* (2015)

$$\alpha = \begin{cases} 1 & R_f \le 0{\cdot}7 \\ R_f^3 - 3R_f^2 + 2R_f + 0{\cdot}7 & 0{\cdot}7 < R_f < 1{\cdot}4 \quad R^2 > 0{\cdot}95 \\ 0{\cdot}364 - \dfrac{3}{5}(R_f - 1{\cdot}4) & R_f \ge 1{\cdot}4 \quad R^2 > 0{\cdot}93 \end{cases} \tag{7}$$

where R^2 is the coefficient of correlation with 95% confidence. Notably, the value of $\alpha = 0{\cdot}7$ (at $D^c_{c35} \approx D^f_{85,SA}$) indicates that only up to 70% fine particles of the mixture participated in sustainable stress transfer, while the remainder may be retained by the self-filtrating process.

Effect of particle–particle contact friction during suffusion failure

Inter-particle contact friction arises from the shape, contact, cohesion, arrangement, packing density and the size of contacting particles, which are conservatively assumed to be spherical and cohesionless in the current study. During suffusion, the fine particles erode through constriction network of stable coarse particles and could make contact with the constriction walls. The additional hydraulic gradient by virtue of inter-particle contact friction is given by (see Appendix for more details)

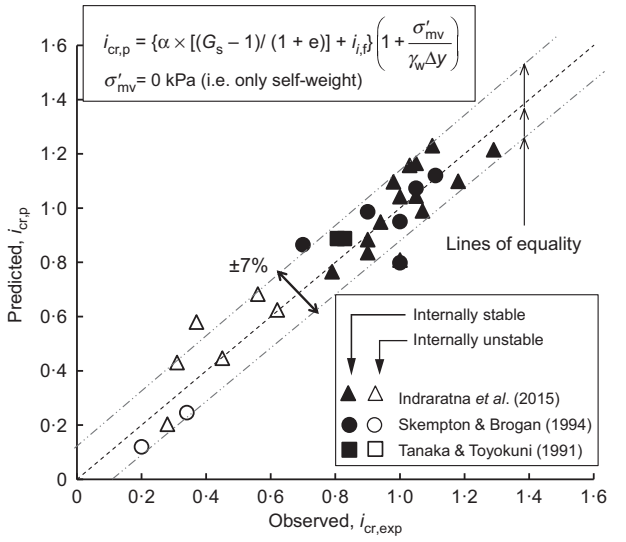

Fig. 11. Comparison between observed and predicted values of critical hydraulic gradients governing the critical onsets

$$i_{pf} = \left[\frac{1}{3} \times \left(\frac{d_a d_b}{d_a + d_b}\right)^2 \frac{\tan \varnothing'}{\gamma_w d_b^2 \delta_y} \times \gamma' h_f\right] \tag{8}$$

where d_a, d_b and δ_y define the representative particle sizes for coarse fraction, fine fraction and the length of an elemental pore channel (D^c_f), as given by the mean particle size for the coarser fraction of the PSD curve (Locke *et al.*, 2001), respectively.

Effect of cell wall–particle contact friction during heave

The particles of an internally stable soil constitute primary fabric that governs sustainable changes in volume due to external loading, while the soil sample behaves like a column or pile (Tanaka & Toyokuni, 1991). The constriction network does not allow fine particles to erode, and the seepage-induced failures could only occur as heave development and occasional piping (in fine sands) at very high i_{cr}, as discussed previously. Consequently, the sample moves as a rigid column due to heave at the critical onset, so the additional gradient due to boundary friction can be given by (Appendix)

$$i_{cf} = \left[\frac{4 \sum_{i=1}^{i=n} [K_0 l_i (0{\cdot}5 \gamma'_{si} h_{fi}) \mu_f]}{\pi \gamma_w h_f D^2}\right] \tag{9}$$

where q_i, μ_f, γ'_{si}, A_{si} and D define skin friction to the movement of a soil, particle–wall contact friction, soil density, circumferential area of the soil layer and cell diameter, respectively. The μ_f values are obtained from modified friction tests (ASTM D1894 (ASTM, 2001a)), that were standardised by consolidated drained direct shear tests (ASTM D3080 (ASTM, 2001b)) on selected samples (Israr *et al.*, 2016b).

Mean vertical effective stress in a soil layer

Given that the effective stress on a soil specimen varies due to a combination of boundary friction and seepage (Moffat & Fannin, 2011), a governing expression can be obtained by applying the limit equilibrium condition between all the forces at the critical onset, thus

$$\partial\sigma/\partial y = \gamma' - i_i \gamma_w - 0{\cdot}5 \eta_f \left(\sigma'_{v,i+1} + \sigma'_{v,i}\right) \tag{10}$$

where $\eta_f = 4\mu_f K_0/D$ is a frictional resistance factor that evolves from K_0 and μ_f. To solve the problem of boundary

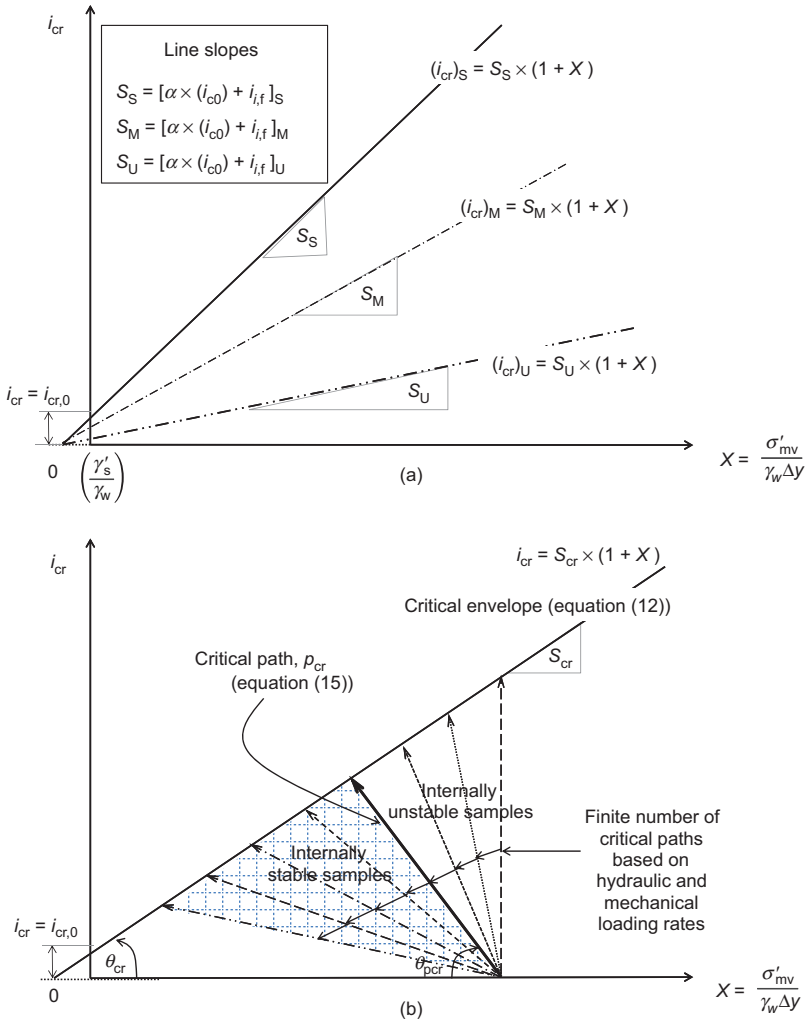

Fig. 12. Illustrations of proposed: (a) critical hydro-mechanical envelopes; (b) critical hydro-mechanical paths governing the inception of internal instability

value (equation (10)), assuming that μ_f is constant along the boundary with a given magnitude of top effective stress ($\sigma'_{v,i+1}$), the effective stress at the bottom ($\sigma'_{v,i}$) of a soil layer, and thus the mean effective stress ($\sigma'_{vm,i}$), can be deduced by the finite-difference discretisation of the sample (Appendix)

$$\sigma'_{vm,i} = \frac{1}{2} \times \left\{ \sigma'_{v,i} \left[1 + (1 - 0{\cdot}5\eta_f \Delta y_i)(1 + 0{\cdot}5\eta_f \Delta y_i)^{-1} \right] + \Delta y_i \gamma' (1 + 0{\cdot}5\eta_f \Delta y_i)^{-1} - \Delta y_i i_i \gamma_w (1 + 0{\cdot}5\eta_f \Delta y_i)^{-1} \right\} \quad (11)$$

CRITICAL ENVELOPES FOR SEEPAGE FAILURE

Inspection of equation (5) suggests that when seepage-induced internal instability begins in granular soils, the relationship between the hydraulic and mechanical constraints would be linear

$$i_{cr} = S_{cr} \times (1 + X) \quad (12)$$

In this dimensionless expression, S_{cr} and X define the values of slope and abscissa for the proposed model, respectively, thus

$$S_{cr} = \alpha \times [(G_s - 1)/(1 + e)] + i_{i,f} \quad (13)$$

$$X = \sigma'_{mv}/\gamma_w \Delta y \quad (14)$$

Equation (12) also indicates that the proposed relationship would be unique for an internally stable or unstable soil, as shown in Fig. 12(a). Notably, when a typical laboratory piping test is used to assess internal stability (i.e. $X = 0$), the y-intercept provides the value of i_{cr} that already incorporates α and $i_{i,f}$-values, depending on whether the soil is stable, marginal, or unstable. For an applied value of σ'_{vt}, a unique value of X is obtained. An internally stable soil follows a hydro-mechanical state that corresponds to $S_{cr} \geq 1$, whereas, marginally and highly unstable soils follow the trends with $S_{cr} < 1$ and $S_{cr} \ll 1$, respectively. This is consistent with the experimental results showing that the hydro-mechanical response for stable, marginal and unstable soils should be unique (e.g. Li & Fannin, 2012; Indraratna *et al.*, 2015). As Fig. 12(b) shows, the critical paths (p_{cr}) evolving from the x-axis at an arbitrary inclination ($\theta_{p,cr}$) and approaching the critical envelopes can be given by the following equation, determined by geometry (see Fig. 12)

$$p_{cr} = \left\{ \left[\alpha \times \left(\frac{G_s - 1}{1 + e} \right) + i_{i,f} \right] \times \left(1 + \frac{\sigma'_{mv,o}}{\gamma_w \Delta y} \right) - \frac{\sigma'_{mv}}{\gamma_w \Delta y} \times \tan \theta_{p,cr} \right\} \quad (15)$$

In the above expression, for a given loading condition, the value of $\theta_{p,cr}$ varies depending on whether the soil is internally stable or unstable. Given that the critical onsets of heave or suffusion in this study were observed at relatively

smaller stresses in internally stable soils compared to the unstable ones, which were still carrying much larger stresses when suffusion occurred. This implies that the inclination of critical paths will be mild for stable soils, and steeper for internally unstable soils (i.e. relatively higher $\theta_{p,cr}$), as shown in Fig. 12(b).

VERIFICATION OF PROPOSED MODEL

A large body of published experimental data from Moffat & Fannin (2011), Trani & Indraratna (2010a, 2010b) and Israr *et al*. (2016b), plus the results of current tests, were used to verify the proposed model. Figs 13(a)–13(d) show the hydro-mechanical paths that led to the critical envelopes of seepage failures for the static tests. Not surprisingly, due to increasing magnitude of σ'_{vt}, the points of initiation continued to shift towards the right-hand side and yield larger critical paths, thereby stabilising the specimens. Nevertheless, each soil sample had a unique inclination of critical paths ($\theta_{p,cr}$) under static loading, although the magnitude of $\theta_{p,cr}$ generally increases with the increasing potential for internal instability, for example 11·9°, 14° and 15·6° for samples A, C and D, respectively (Table 2). As Figs 13(e)–13(h) show, the point of initiation is almost the same because the cyclic load has a constant magnitude ($\sigma'_{min} = 30$ and $\sigma'_{max} = 70$ kPa). However, the magnitude of $\theta_{p,cr}$ increases as the cyclic loading increases in frequency (see Table 2), and the critical paths become shorter. This indicates that the extremely premature failure that develops at a higher frequency loading is fully consistent with the experimental observations made in this study.

Figures 14(a)–14(d) present the critical envelopes obtained from the proposed model and the associated experimental data from published studies as well as from this current work that are used for validation. The i_{cr} plotted against the dimensionless mechanical number X indicates the critical envelopes. As Table 2 shows, each soil sample follows a critical envelope at a unique critical inclination (θ_{cr}), depending on its geometrical and physical characteristics for given hydraulic and mechanical loading. Fig. 14(a) shows a close agreement between the model predictions and the experimental results of Moffat & Fannin (2011), who examined the internal stability of broadly and gap graded soils subjected to static load under upward and downward flow conditions. Fig. 14(b) presents an interesting analysis for the test data of Trani & Indraratna (2010a, 2010b) under cyclic loading, where theoretical envelopes are plotted for four different filters (F1–F4) and the self-filtering layer (F1-B). Filters F2 and F4 showed internal instability under cyclic loading, whereas the self-filtering layer F1-B was internally stable. The experimental points are also plotted for the applied hydraulic gradient $i_a \approx 10$ and the given stress conditions. All the filters plotted well below their respective critical envelopes and were deemed internally stable except F4; however, the experimental results revealed that F2 and F4 were internally unstable (Trani & Indraratna, 2010a, 2010b). This discrepancy for F2 may be attributed to the development of excess pore pressure and agitation by cyclic loading that may have caused suffusion to occur. Figs 14(c) and 14(d) present comparisons between the experimental results and theoretical predictions for the static and cyclic piping test data of Israr *et al*. (2016b) and the current study, respectively, where there are close agreements between the theory and experimental results.

As Fig. 14 shows, the lines originate from the y-axis at an intercept equal to $i_{cr,0}$ (at $\sigma'_{vt} = 0$ kPa) and progress at a unique inclination (θ_{cr}) in the form of critical envelopes where the magnitude of θ_{cr} is directly proportional to the internal stability of the soil. For instance, the orders of internal stability potential from the proposed model were consistent with those observed experimentally (highest to lowest), that is T-0 > T-5 > C-30 > C-20 (Moffat & Fannin, 2011), F3 > F1 > F2 > F4 > F1-B (Trani & Indraratna, 2010a, 2010b), C > F > G (Israr *et al*., 2016b) and A > B > C > D (current study). Regardless of the static or cyclic load applied during hydraulic tests, the experimental data which plot along these critical envelopes agree closely with the proposed theory, albeit with small discrepancies between the laboratory results and theoretical predictions. In essence, for the given hydraulic (i_a) and mechanical (σ'_v) values, the geometrical (PSD and constriction size distribution) and physical (R_d and μ_f) factors in tandem control the seepage-induced response of soils, and they follow unique hydro-mechanical envelopes and corresponding paths that govern the critical onsets of internal instability.

LIMITATIONS OF THIS STUDY

This study is focused on seepage analysis of granular soils under one-dimensional upward flow, which in practice would simulate real-life filters, for example, those commonly used in transportation embankments and at the downstream side of dams. As a practical tool for practitioners, visual guides in the form of well-defined hydro-mechanical paths leading to critical hydro-mechanical envelopes for internal instability have been proposed herein. Notably, the hydro-mechanical equilibrium and the non-horizontal seepage paths in full-scale embankment dams may be significantly different from those considered here for simplified laboratory (often one-dimensional) equipment. As an example, deposition of eroded and displaced fine particles is easily understood in the case of horizontal seepage (Skempton & Brogan, 1994). Nevertheless, as a common limitation for most experimental studies, the scale of the laboratory simulations may not be comparable with the actual dimensions of full-scale engineering problems. Therefore, the applicability of the proposed charts to field problems should be validated further, but they can still be recommended as preliminary guides prior to detailed analysis.

CONCLUSIONS

An experimental investigation into the internal stability of a select range of compacted soils was carried out, and a theoretical model to govern the occurrence of heave and suffusion in soils under static and cyclic loading was proposed. On the basis that the proposed model agreed closely with the experimental results, the following conclusions could be drawn.

The phenomena of stress reduction in unstable soils triggered suffusion of fine particles at relatively smaller i_{cr} and larger associated σ'_{mv} that changed their PSD, whereas internally stable soils exhibited heave at larger i_{cr} and smaller σ'_{mv} with little changes to their PSD. For instance during tests at $\sigma'_{vt} = 50$ kPa, soil A experienced heave at $i_{cr} = 36$ and $\sigma'_{mv} = 6$ kPa, whereas soil D exhibited suffusion at $i_{cr} = 22$ and $\sigma'_{mv} = 23{\cdot}2$ kPa. Similarly, heave developed in soil C at $i_{cr} = 30$ and $\sigma'_{mv} = 11$ kPa during static tests, while suffusion occurred at $i_{cr} = 24$ and $\sigma'_{mv} = 22$ kPa during cyclic testing at 5 Hz. The internal and boundary frictions were observed to influence the magnitudes of i_{cr} and σ'_{mv} during suffusion and heave, respectively.

As functions of PSD and frictional characteristics of current specimens, the seepage failures commenced at specific hydro-mechanical boundaries. For instance, heave and suffusion developed in samples A and D at specific combinations of i_{cr} and σ'_{mv} that could be defined by linear relationships with specific critical inclinations (θ_{cr}) of 54·5°

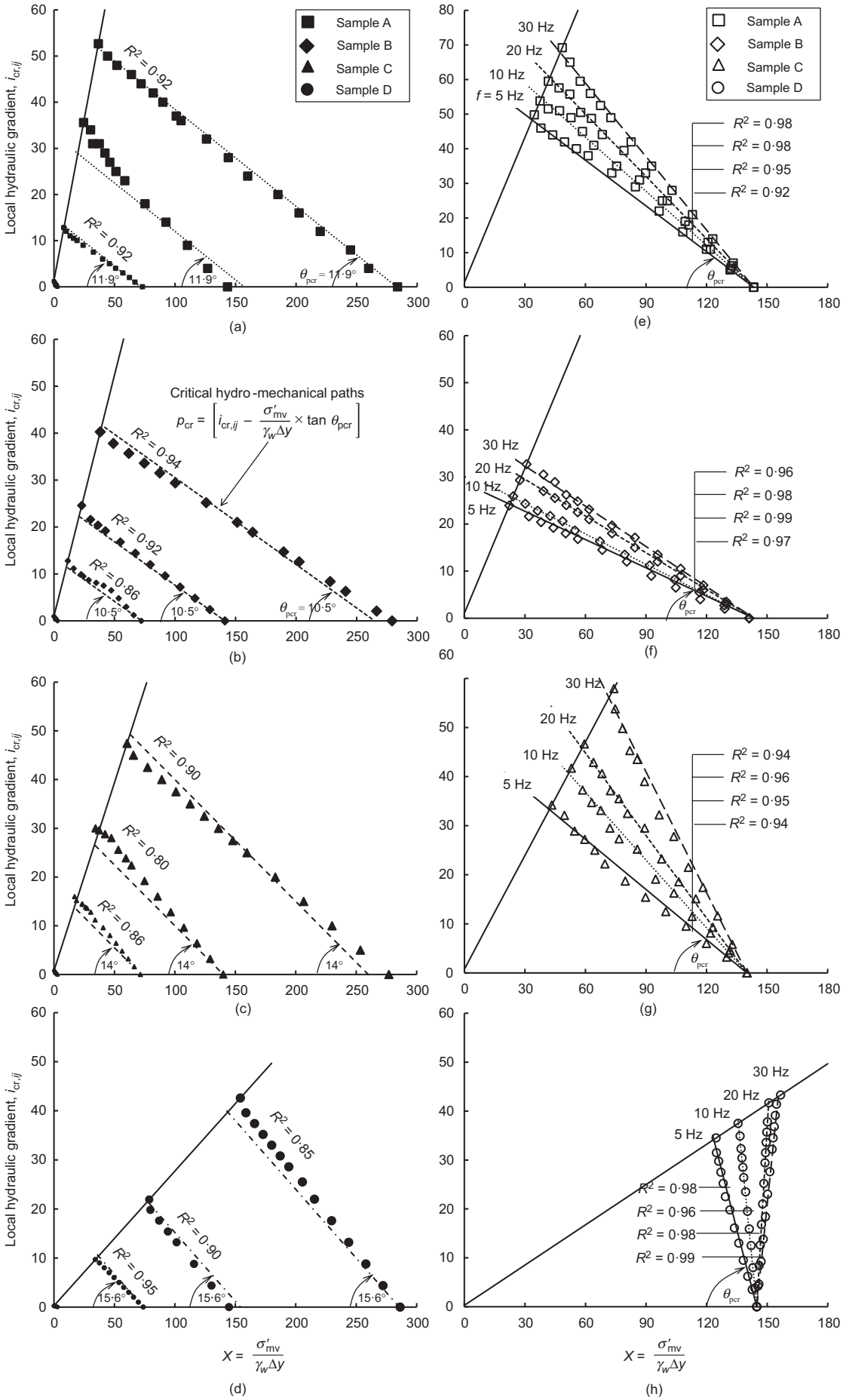

Fig. 13. Critical hydro-mechanical paths for current test samples under static loading and cyclic loading: (a) A-S; (b) B-S; (c) C-S; (d) D-S; (e) A-C; (f) B-C; (g) C-C; (h) D-C

Table 2. Observed inclinations of critical envelopes and paths for the current samples

Sample ID	Inclination of critical envelope, θ_{cr}	Inclination of critical envelope, $\theta_{p,cr}$				
		$f = 0$ Hz	$f = 5$ Hz	$f = 10$ Hz	$f = 20$ Hz	$f = 30$ Hz
A	1·4	11·9	23·8	27·5	31	35·3
B	1·03	10·5	11·3	12·1	14·6	15·9
C	0·77	14	18·8	24·7	29·3	39·4
D	0·27	15·6	58·2	76·4	98·1	104

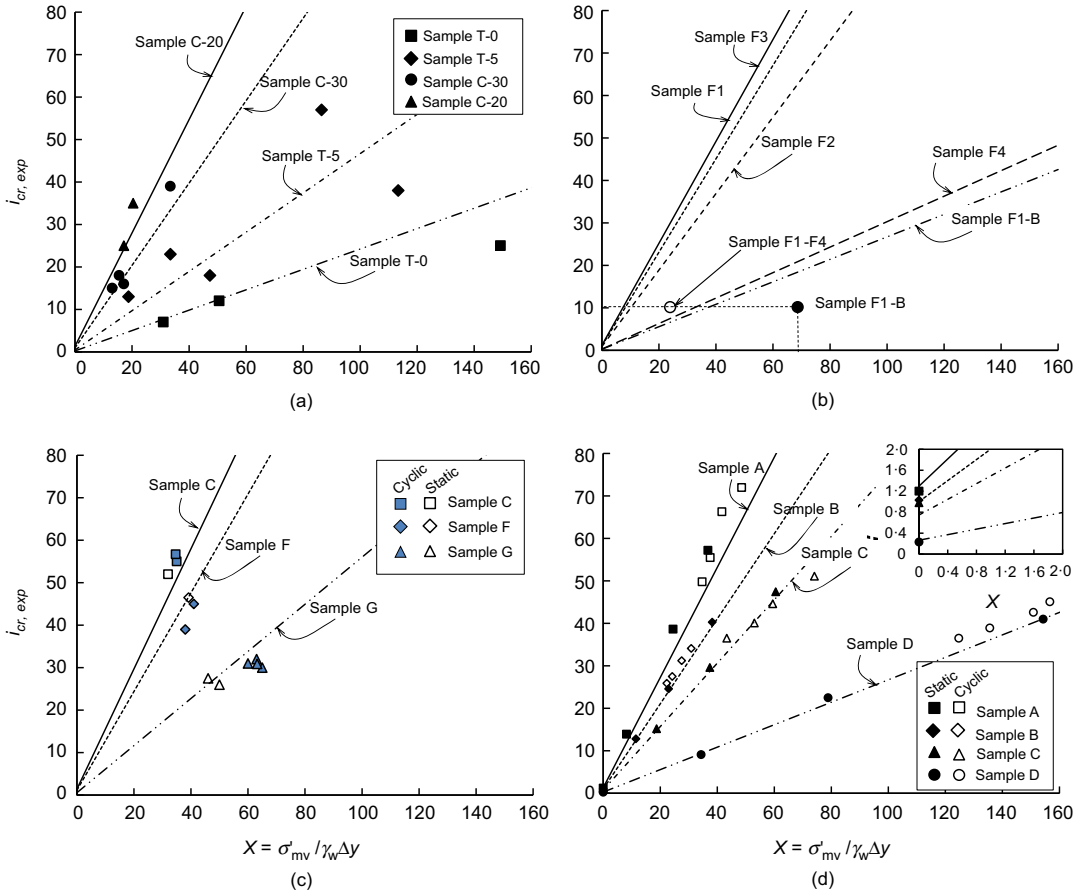

Fig. 14. Model validation using data from: (a) Moffat & Fannin (2011); (b) Trani & Indraratna (2010a, 2010b); (c) Israr *et al.* (2016b); (d) current study

and 15·1°, respectively. Similarly, samples B and C suffered from seepage failures at θ_{cr} of 45·9° and 37·6°, respectively. In this study, the inception of heave and suffusion was modelled by combining the effects of i_{cr}, σ'_{mv}, stress reduction and friction that agreed closely with the experimental results.

The proposed model yielded specific critical envelopes and paths with their respective inclinations (θ_{cr} and $\theta_{p,cr}$), depending upon the soil types and loading conditions. Each soil possessed a unique inclination of its critical path $\theta_{p,cr}$, which varied depending upon the loading condition. For example, values of $\theta_{p,cr}$ of 11·9°, 10·5°, 14°, and 15·6° for soils A, B, C and D, respectively, that did not change under static loading, increased proportionally with the cyclic loading frequency. Increase in σ'_{vt} tended to stabilise the soil by extending the lengths of the critical paths, whereas higher loading frequencies tended to destabilise the soil by shortening the critical paths (i.e. higher $\theta_{p,cr}$) and hence the i_{cr} values.

In place of PSD-based geometrical 'stable/ unstable' bifurcation, the extent and potential of internal instability could be described by the inclinations (θ_{cr}) of critical envelopes which govern the occurrence of soil instability. Unlike existing criteria, which tend to be unsafe under cyclic conditions, the current model successfully assessed the potential of instability. For instance, the predicted order of stability is fully consistent with that observed during hydraulic testing for the reported data, regardless of the loading conditions, as demonstrated on the basis of data sourced from past literature and the current study.

Although assessed as stable by the existing geometrical criteria, the non-uniform broadly and gap-graded soils ($C_u > 10$) can be likely to suffer from suffusion under cyclic loading, and therefore they must be selected carefully. Although the current study provides a greater insight to the internal stability of granular media, further research is still needed to expand the scope of the current model to encompass a wider array of broadly and gap-graded soils.

ACKNOWLEDGEMENTS

Financial support received by the second author through scholarships from University of Engineering and Technology

Lahore (Pakistan) and University of Wollongong (UOW) is appreciated. Technical staff support at UOW during laboratory tests is also acknowledged.

APPENDIX

Expression for hydraulic gradient due to particle–particle contact

The effective confining stress acting on the soil is a function of top and bottom vertical stresses (0 and $\gamma' h_f$, respectively) and the internal friction angle ($\varnothing'$). For $\sigma'_{mv} = 0{\cdot}5\gamma' h_f$, where two non-rigid and smooth spheres A and B make contact with radii r_a and r_b, respectively (Fig. 15), the contact area is expressed by an imaginary circle of radius $r_c = [(1/r_a) + (1/r_b)]^{-1}$. Assuming $\sigma(r_i) = \sigma'_{c0}$, the normal force at the contact gives

$$F_N = 2\pi \int_0^{r_e} \sigma(r_i) r_i \, dr_i = \pi r_e^2 \gamma' h_f / 3 \tag{16}$$

where r_c should be $\leq r_e (= (3r_c F_N / 2E_c)^{1/3})$, that is the maximum permissible linear elastic contact radius (Hertz, 1882), with $E_c = 2 \times \left[(1 - v_a^2/E_a) + (1 - v_b^2/E_b)\right]^{-1}$. Note that the value of r_c should simultaneously satisfy the expressions for r_e and F_N. Assuming that $r_c < r_e$ for saturated conditions, the contact friction between two spheres may then be expressed as a function of F_N and $\varnothing'$, for which the equilibrium between the frictional and hydrodynamic forces ($F_s = F_h$) gives

$$\frac{2\pi}{3} r_c^2 \tan \varnothing' \gamma' h_f / 2 = \frac{\pi}{4} \gamma_w d_b^2 \delta_y \, i \tag{17}$$

Rearrangement of the above equation (17) can give equation (8).

Expression for hydraulic gradient due to wall–particle contact

Consider a soil column of thickness h_f and cross-sectional area A_f subject to a surcharge pressure q_s and seepage force caused by a hydraulic gradient i, as shown in Fig. 15. If Q_f, Q_b and F_{sp} define the skin friction along the cell wall, the total load at the base and seepage force on the soil column, respectively, the balance of forces at the onset of heave gives

$$F_{sp} = Q_b + Q_f \tag{18}$$

$$i \gamma_w h_f A_f = \sigma'_{vt} A_f + \sum_{i=1}^{i=n} q_i A_{si} \tag{19}$$

$$i_{cr,p} = \left[\frac{\sigma'_{vt}}{\gamma_w h_f} + \frac{\sum_{i=1}^{i=n} q_i A_{si}}{\gamma_w h_f A_f} \right] \tag{20}$$

where $i_{cr,p}$ is the critical hydraulic gradient for heave failure. Equation (20) has two components, where the former represents

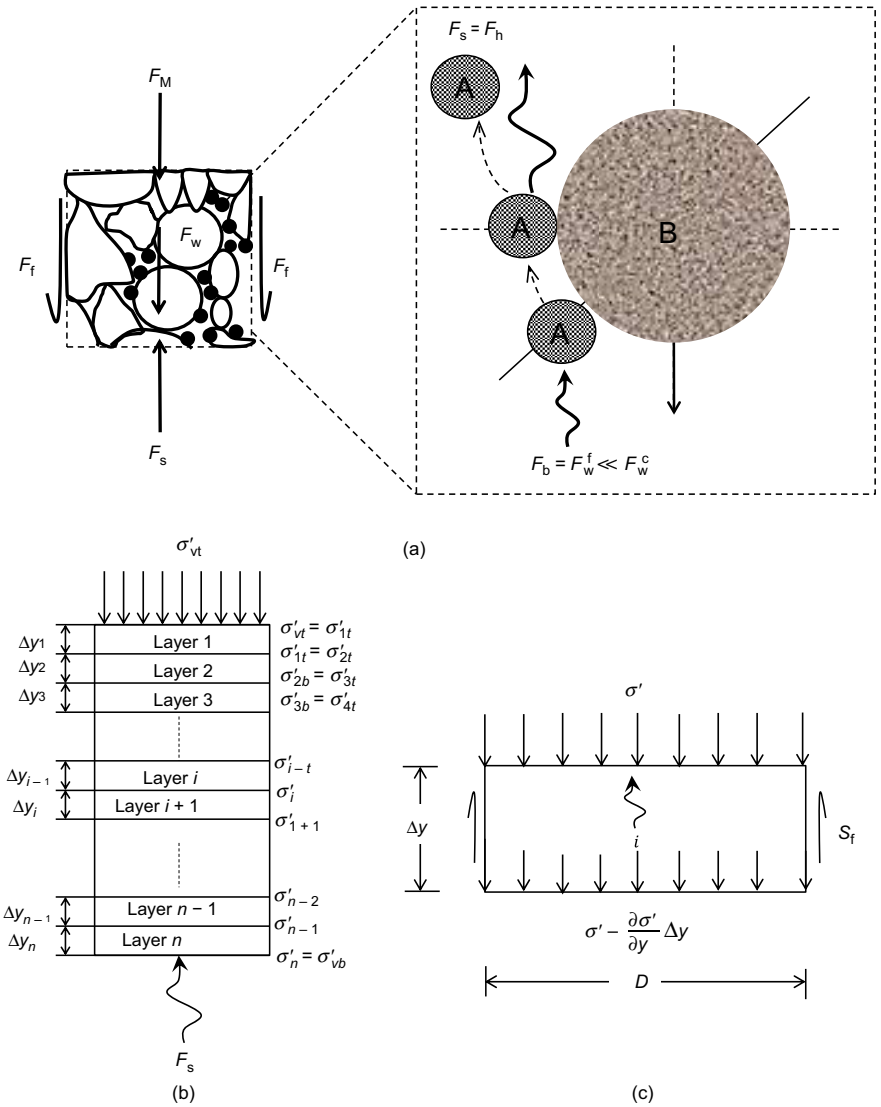

Fig. 15. Idealised soil layer: (a) subjected to various loads; (b) layer discretisation to facilitate frictional resistance calculations; (c) effective stress distribution diagram for soil layer

the hydraulic gradient due to σ'_{vt} that is neutralised by buoyancy at the onset of heave, while the latter represents skin friction due to wall–particle contact and the self-weight of the soil column. By eliminating the term containing σ'_{vt} from the right-hand side of equation (20), it can be simplied further to obtain

$$i_{cf} = \left[\frac{4\sum_{i=1}^{i=n}[K_0 l_i(0{\cdot}5\gamma'_{si}h_{fi})\mu_f]}{\pi\gamma_w h_f D^2}\right] \tag{21}$$

Expression for mean effective stress

At the critical onset, the limit equilibrium between all the forces acting on a layer of soil gives

$$F_M + F_W + F_f + F_S = 0 \tag{22}$$

where F_M, F_W, F_f and F_S defines the sum of forces due to vertical effective stresses, the effective weight of the layer of soil, the frictional resistance of the cell-wall (boundary) and seepage stresses due to the hydraulic gradient, respectively, where

$$F_M = -0{\cdot}25\pi D^2(\partial\sigma/\partial y)\mathrm{d}y \tag{23}$$

$$F_W = 0{\cdot}25\pi D^2\gamma'\mathrm{d}y \tag{24}$$

$$F_f = \pi D\mu K_0\sigma'_{mv}\mathrm{d}y = 0{\cdot}5\pi D\mu K_0\left(\sigma'_{v,i+1} + \sigma'_{v,i}\right)\mathrm{d}y \tag{25}$$

$$F_S = 0{\cdot}25\pi D^2 i_i\gamma_w\mathrm{d}y \tag{26}$$

Substituting equations (23)–(26) into equation (22) and simplifying for upward flow and frictional resistance against σ'_{vm}, the governing expression for stress reduction is given by

$$\partial\sigma/\partial y = \gamma' - i_i\gamma_w - 0{\cdot}5\eta_f\left(\sigma'_{v,i+1} + \sigma'_{v,i}\right) \tag{27}$$

where $\eta_f = 4\mu_f K_0/D$ is the frictional resistance factor that evolves from K_0 and μ_f. To solve the boundary value problem (equation (27)), assuming that μ_f is constant along the boundary with given magnitude of top effective stress ($\sigma'_{v,i+1}$), the effective stress at the bottom ($\sigma'_{v,i}$) of a soil layer can be deduced by the finite-difference discretisation of a soil column

$$\left(\sigma'_{v,i+1} - \sigma'_{v,i}\right)/\Delta y_i = \gamma' - i_i\gamma_w - 0{\cdot}5\eta_f\left(\sigma'_{v,i+1} + \sigma'_{v,i}\right) \tag{28}$$

The effective stress in the soil layer is now given by

$$\begin{aligned}\sigma'_{v,i+1} = \Big[&\sigma'_{v,i}(1 - 0{\cdot}5\eta_f\Delta y_i)(1 + 0{\cdot}5\eta_f\Delta y_i)^{-1} \\ &+\Delta y_i\gamma(1 + 0{\cdot}5\eta_f\Delta y_i)^{-1} - \Delta y_i i_i\gamma_w(1 + 0{\cdot}5\eta_f\Delta y_i)^{-1}\Big]\end{aligned} \tag{29}$$

The mean effective stress in the soil layer is then given by

$$\sigma'_{mv} = 0{\cdot}5\left(\sigma'_{v,i+1} + \sigma'_{v,i}\right) \tag{30}$$

Substituting equation (29) in equation (30), an expression for the mean effective stress may be obtained as follows

$$\begin{aligned}\sigma'_{vm,i} = \frac{1}{2}\times\Big\{&\sigma'_{v,i}\Big[1 + (1 - 0{\cdot}5\eta_f\Delta y_i)(1 + 0{\cdot}5\eta_f\Delta y_i)^{-1}\Big] \\ &+\Delta y_i\gamma'(1 + 0{\cdot}5\eta_f\Delta y_i)^{-1} - \Delta y_i i_i\gamma_w(1 + 0{\cdot}5\eta_f\Delta y_i)^{-1}\Big\}\end{aligned} \tag{31}$$

Note that equation (31) is equation (11) in the main text.

NOTATION

A_f, A_{si}	cross-sectional area (m^2)
C_d	coefficient of drag
C_u	coefficient of uniformity
D	cell diameter
D, d	particle size (mm)
$D^f_{85,\,SA}$	particle size at 85% finer by surface area (mm)
d^f_{85} and D^c_{c35}	particle size at 85% finer and controlling constriction of coarse fraction (mm)
$d_{85,Base}$ and $D_{c35,Filter}$	base particle at 85% finer and controlling constriction of filter (mm)
E_b	Young's modulus for particle B (GPa)
E_c	Young's modulus (GPa)
F_M, F_W, F_f and F_S	forces due to vertical effective stresses, the effective weight of the layer of soil, the frictional resistance of the cell–wall (boundary) and seepage stresses due to the hydraulic gradient, respectively
f	cyclic loading frequency (Hz)
H^t_w	external head loss measured across inflow and outflow transducers
h	specimen depth
h_f	depth of sample
h^t_w	internal head losses measured across differential pore pressure transducers
i_a, i_{exp}, i_{ij} and i_{cr}	applied, experimental, local and critical hydraulic gradients, respectively
$i_{cr,exp}$, $i_{cr,th}$ and $i_{cr,p}$	experimental, theoretical and predicted critical gradients, respectively
$i_{\Delta u}$	additional hydraulic gradient
K_g	dimensionless geometrical number
K_0	coefficient of earth pressure at rest
k_s	saturated permeability of soil (m/s)
N_m	dimensionless mechanical number
n	porosity (%)
p_{cr}	critical path
p_w	hydraulic pressure (kPa)
Q_b and Q_f	base load and skin friction, respectively (kN)
Q_e and T_e	effluent flow rate and turbidity, respectively (l/min)
q_i	surcharge over a soil layer i (kPa)
R_d	relative density
R_f	retention ratio of Indraratna *et al.* (2015)
R_n	Reynold's number
r	radius of an imaginary soil particle or a contact circle (mm)
r_c	radius of an imaginary contact circle (mm)
r_e	equivalent radius of imaginary contact circle (mm)
S_{cr}	slope of critical envelope
S_S, S_M, S_U	line slopes
t	time (min)
v, ε_a, α	Poisson ratio, axial strain and stress reduction factor, respectively
γ'_{si}	soil density
γ_w	unit weight of water (kN/m^3)
Δy	soil layer
δ_y	length of hydrodynamic channel (mm)
θ_{cr}, $\theta_{p,cr}$	inclinations for critical envelope and critical path, respectively
μ_f, η_f	friction factors
σ_b	buoyancy stress
σ_d	drag stress
σ'_c, σ'_{c0}, $\sigma'_{v,mean}$, σ_{vt}	contact, confining, mean effective and total vertical stresses (kPa)
σ_h	hydro-dynamic stress
σ_s	seepage stress (kPa)
τ_f	contact or boundary friction (kPa)
$\varnothing'$	drained angle of internal friction (degrees)

REFERENCES

ASTM (2001a). ASTM D1894-01: Standard test method for static and kinetic coefficients of friction of plastic film and sheeting. West Conshohocken, PA, USA: ASTM International.

ASTM (2001b). ASTM D3080-11: Standard test method for direct shear test of soils under consolidated drained conditions. West Conshohocken, PA, USA: ASTM International.

ASTM (2006). ASTM D4253-06: Standard test methods for maximum index density and unit weight of soils using a vibratory table. West Conshohocken, PA, USA: ASTM International.

Batchelor, G. K. (1967). *An introduction to fluid dynamics*. Cambridge, UK: Cambridge University Press.

Fourie, A. B., Copeland, A. M. & Barrett, A. J. (1994). Optimization of the as-placed properties of hydraulic backfill. *J. S. Afr. Inst. Min. Metall.* **94**, No. 8, 199–210.

Hertz, H. R. (1882). On contact between elastic bodies (collected works). *J. Reine u. Angew. Math.* **92**, 156–171 (in German).

Indraratna, B., Israr, J. & Rujikiatkamjorn, C. (2015). Geometrical method for evaluating the internal instability of granular filters based on constriction size distribution. *J. Geotech. Geoenviron. Engng* **141**, No. 10, 04015045.

Indraratna, B., Israr, J. & Rujikiatkamjorn, C. (2016). Closure of geometrical method for evaluating the internal instability of granular filters based on constriction size distribution. *J. Geotech. Geoenviron. Engng* **142**, No. 9, 07016022.

Israr, J. (2016). *Internal instability of granular filters under cyclic loading*. PhD thesis, University of Wollongong, Wollongong, Australia.

Israr, J. & Indraratna, B. (2017). Internal stability of granular filters under static and cyclic loading. *J. Geotech. Geoenviron. Engng* **143**, No. 6, 04017012.

Israr, J., Indraratna, B. & Rujikiatkamjorn, C. (2016a). Internal stability of drainage layer in railway foundation under cyclic loading. *Proceedings of the 7th civil engineering conference in the Asian region, (ASCE)*, Waikiki, HA, USA

Israr, J., Indraratna, B. & Rujikiatkamjorn, C. (2016b). Laboratory modelling of the seepage induced response of granular soils under static and cyclic conditions. *Geotech. Testing J.* **39**, No. 5, 1–18.

Kenney, T. C. & Lau, D. (1985). Internal stability of granular filters. *Can. Geotech. J.* **22**, No. 2, 215–225.

Kezdi, A. (1979). *Soil physics.* Amsterdam, the Netherlands: Elsevier Scientific.

Lafleur, J., Mlynarek, J. & Rollin, A. (1989). Filtration of broadly graded cohesionless soils. *J. Geotech. Engng* **115**, No. 12, 1747–1768.

Langroudi, F. M., Soroush, A., Tabatabaie, S. P. & Shafipour, R. (2013). Stress transmission in internally unstable gap-graded soils using discrete element modeling. *Powder Technol.* **247**, No. 1, 161–171.

Li, M. & Fannin, R. J. (2008). Comparison of two criteria for internal stability of granular soil. *Can. Geotech. J.* **45**, No. 9, 1303–1309.

Li, M. & Fannin, R. J. (2012). A theoretical envelope for internal instability of cohesionless soil. *Géotechnique* **62**, No. 1, 77–80, http://dx.doi.org/10.1680/geot.10.T.019.

Locke, M., Indraratna, B. & Adikari, G. (2001). Time-dependent particle transport through granular filters. *J. Geotech. Geoenviron. Engng* **127**, No. 6, 521–529.

Moffat, R. & Fannin, R. J. (2011). A hydromechanical relation governing the internal stability of cohesionless soil. *Can. Geotech. J.* **48**, No. 3, 413–424.

Scheuermann, A., Steeb, H. & Kiefer, J. (2010). Internal erosion of granular materials-identification of erodible fine particles as a basis for numerical calculations. *Proceedings of 9th HSTAM international congress on mechanics*, Limassol, Cyprus, pp. 275–282.

Shire, T. & O'Sullivan, C. (2013). Micromechanical assessment of an internal stability criterion. *Acta Geotechnica* **8**, No. 1, 81–90.

Shire, T., O'Sullivan, C., Hanley, K. J. & Fannin, R. J. (2014). Fabric and effective stress distribution in internally unstable soils. *J. Geotech. Geoenviron. Engng* **140**, No. 12, 04014072.

Skempton, A. W. & Brogan, J. M. (1994). Experiments on piping in sandy gravels. *Géotechnique* **44**, No. 3, 449–460, http://dx.doi.org/10.1680/geot.1994.44.3.449.

Smith, J. L. & Bhatia, S. K. (2010). Minimizing soil erosion with geosynthetic rolled erosion control products. *Geo-Strata – Geo Inst.* **14**, No. 4, 50–53.

Tanaka, T. & Toyokuni, E. (1991). Seepage failure experiments on multi layered sand columns. *Soils Found.* **31**, No. 4, 13–36.

Taylor, H. F., O'Sullivan, C. & Sim, W. W. (2015). A new method to identify void constrictions in micro-CT images of sand. *Comput. Geotech.* **69**, 279–290.

Terzaghi, K. (1939). Soil mechanics–a new chapter in engineering science. *J. Instn Civ. Engrs (UK)* **12**, No. 7, 106–141.

Trani, L. D. O. & Indraratna, B. (2010a). Assessment of subballast filtration under cyclic loading. *J. Geotech. Geoenviron. Engng* **136**, No. 11, 1519–1528.

Trani, L. D. O. & Indraratna, B. (2010b). Use of impedance probe for estimation of porosity changes in saturated granular filters under cyclic loading: calibration and application. *J. Geotech. Geoenviron. Engng* **136**, No. 10, 1469–1474.

Vaughan, P. & Soares, H. (1982). Design of filters for clay cores of dams. *J. Geotech. Engng Div.* **108**, No. 1, 17–31.

Xiao, M., Reddi, L. N. & Steinberg, S. (2006). Effect of vibrations on pore fluid distribution in porous media. *Transp. Porous Media* **62**, No. 2, 187–204.

Zou, Y., Chen, Q., Chen, X. & Cui, P. (2013). Discrete numerical modelling of particle transport in granular filters. *Comput. Geotech.* **32**, No. 5, 340–357.